Supplementary material for "Quantifying the buffering of oceanic oxygen isotopes at ancient midocean ridges"

Yoshiki Kanzaki

S1. Two-dimensional distributions of solid-rock and porewater δ^{18}O with different spreading rates and ocean depths

Figs. S1 and S2 provide 2D distributions of solid-rock and porewater δ^{18}O with different spreading rates (1×10^{-2}, 9×10^{-2} and 30×10^{-2} m yr^{-1}) and ocean depths (1 and 5 km) considered for the Precambrian in Section 3.3.

S2. Sensitivity to permeability distribution

Permeability distribution significantly affects hydrothermal flow geometry and intensity and thus ^{18}O distributions within oceanic crust. However, as long as the model can reproduce modern observations with a certain permeability distribution, general conclusions given in the main text remain valid. To demonstrate this, here we consider three different permeability distributions: case 1, which assumes the standard parameterization for permeability (Section 2.1); case 2, which assumes a larger scale-length (500 m) for the e-fold permeability decrease with otherwise the same parameterization as in case 1; and case 3, which assumes larger values for both the scale length (500 m) and the permeability at the crust/ocean interface ($10^{-11.3}$ m^2). The permeability is largest in case 3 and decreases from case 3 to 1 at any depths (Fig. S3). Consistently, water exchange increases from case 1 to 3 (1.2×10^{13}, 4.9×10^{13} and 1.2×10^{14} kg yr^{-1} in cases 1–3, respectively) with relatively invariant total heat flux at 0.74×10^{12} W (Fig. S4). Despite the significant difference especially in the water exchange, simulated δ^{18}O distributions are largely consistent with observations in all three cases (Fig. S5). In any of the three cases, oceanic rocks are relatively insensitive to seawater δ^{18}O (Fig. S5). Correspondingly, seawater-δ^{18}O buffering is relatively weak (Fig. S6): -0.4×10^9, -0.7×10^9 and -0.7×10^9 mol yr^{-1} ‰$^{-1}$ in cases 1–3, respectively (cf. Fig. 6).

S3. Sensitivity to oxygen isotope exchange kinetics

Water-rock interactions in the field can be slower than those in the laboratory by a factor of up to 10^3 (White and Brantley, 2003; Wallmann et al., 2008). Accordingly, while the rate constant at reference temperature (5 °C) for oxygen isotope exchange (denoted as k_{ex}^{ref} here) adopted for the present study ($k_{ex}^{ref} = 10^{-8.5}$ mol^{-1} kg yr^{-1}; Eq. (7) in Section 2.2) is comparable to the range ($10^{-6.6}$–$10^{-7.2}$ mol^{-1} kg yr^{-1}) extrapolated from laboratory results (Cole et al., 1987) with the specific surface area of marine basalt (Nielsen and Fisk, 2010), the k_{ex}^{ref} value plausible in the field can differ from the standard value (i.e., $10^{-8.5}$) by a factor of 10. Additional numerical experiments with k_{ex}^{ref} varied in the range of $10^{-7.5}$–$10^{-9.5}$ mol^{-1} kg yr^{-1} (Figs. S7 and S8) with otherwise the standard modern configuration, however, suggest that general results and conclusions are not affected by this uncertainty; the buffering intensity (i.e., slope in Fig. S8) is -0.4×10^{9} mol yr^{-1} ‰$^{-1}$, not significantly different from that in the standard simulation. Results for solid rock δ^{18}O are also comparable to Oman ophiolite data although with the standard k_{ex}^{ref} value, observed data points are better reproduced (Fig. S7).

S4. Effects of off-axis hydrothermal fluid circulation

The numerical model presented in the main text is designed to simulate hydrothermal fluid circulation and oxygen isotopes relatively close to midocean ridges, not for off-axis simulations (Stein et al., 1995). This is reasonable given that oxygen isotopic composition of oceanic rocks is determined within less than 10 million years from the ridge axis (Muehlenbachs, 1979). Nonetheless, to evaluate the effects of off-axis hydrothermal fluid circulation on the oxygen-isotope buffering across a wider oceanic crust, an additional experiment (referred to as "off-axis experiment 1") was conducted with a wider calculation domain, 300 km (cf. 30 km in the standard simulation), and imposing artificial pressures from overlying sediments to cause off-axis water flows (Fisher and Becker, 2000). Additional pressures of 10 MPa are imposed upon 25 MPa of default hydrostatic pressure (with the crust/ocean interface at 2.5 km depth) in regions of 30–50, 70–100, 125–150, 175–200, 225–250 and 275–300 km from the ridge axis. The larger pressures imposed upon wider distance-intervals than inferred by Fisher and Becker (2000) were necessary for the numerical stability in the wider calculation domain with limited resolution. Resulting total water exchange is 5.3×10^{15} kg yr^{-1}, which agrees with the estimated range (4×10^{14}–8×10^{15} kg yr^{-1}) for low temperature hydrothermal fluid flux (Elderfield and Schultz, 1996; Coogan and Gillis, 2013). However, cumulative heat flux in off-axis experiment 1 is 0.75×10^{12} W, smaller than the observation within 9 Ma (corresponding to 270 km with 3×10^{-2} m yr^{-1} spreading rate) from the ridge axis, $3.8(\pm2.1) \times 10^{12}$ W (Stein and Stein, 1994) (Fig. S9). To consider a system with a more heat flux closer to the observation average, another experiment (referred to as "off-axis experiment 2") was performed assuming 400 °C at the bottom of the wider calculation domain (cf. Iyer et al., 2010) with the same pressures from overlying sediments as those in off-axis experiment 1. Off-axis experiment 2 yields 3.5×10^{12} W of cumulative heat flux and 5.6×10^{14} kg yr^{-1} of total water exchange, both of which are consistent with the observations (Stein and Stein, 1994; Elderfield and Schultz, 1996; Coogan and Gillis, 2013) (Fig. S9).

Oxygen isotope behaviors in the off-axis experiments are similar to those described in the main text (Figs. S10–S13). The buffering intensity (i.e., slope in Fig. S13) is -0.5×10^{9} and -0.4×10^{9} mol yr^{-1} ‰$^{-1}$ in off-axis experiments 1 and 2, respectively, not so different from the standard simulation without off-axis water flows (Fig. S13).

Solid rock $\delta^{18}O$ profiles at 300 km (or 10 Ma) show relative insensitivity to seawater $\delta^{18}O$, as observed in the standard case. The only notable difference from the standard case is that low-temperature isotope exchange reactions are enhanced relative to high-temperature reactions in the two off-axis experiments (Figs. S10–S13). It is clear from the two experiments that the results and conclusions given in the main text are valid whether or not off-axis water flows are included.

References

Cole, D. R., Mottl, M. J., and Ohmoto, H. (1987). Isotopic exchange in mineral-fluid systems. II. oxygen and hydrogen isotopic investigation of the experimental basalt-seawater system. *Geochimica et Cosmochimica Acta*, 51(6):1523–1538.

Coogan, L. A. and Gillis, K. M. (2013). Evidence that low-temperature oceanic hydrothermal systems play an important role in the silicate-carbonate weathering cycle and long-term climate regulation. *Geochemistry, Geophysics, Geosystems*, 14(6):1771–1786.

Elderfield, H. and Schultz, A. (1996). Mid-ocean ridge hydrothermal fluxes and the chemical composition of the ocean. *Annual Review of Earth and Planetary Sciences*, 24(1):191–224.

Fisher, A. and Becker, K. (2000). Channelized fluid flow in oceanic crust reconciles heat-flow and permeability data. *Nature*, 403(6765):71.

Fisher, A. T. (1998). Permeability within basaltic oceanic crust. *Reviews of Geophysics*, 36(2):143–182.

Iyer, K., Rüpke, L. H., and Morgan, J. P. (2010). Feedbacks between mantle hydration and hydrothermal convection at ocean spreading centers. *Earth and Planetary Science Letters*, 296(1-2):34–44.

Muehlenbachs, K. (1979). The alteration and aging of the basaltic layer of the seafloor: Oxygen isotope evidence from DSDP/IPOD Legs 51, 52, and 53. *Int. Repts. DSDP*, 51:1159–1167.

Nielsen, M. E. and Fisk, M. R. (2010). Surface area measurements of marine basalts: implications for the subseafloor microbial biomass. *Geophysical Research Letters*, 37(15).

Stein, C. A. and Stein, S. (1994). Constraints on hydrothermal heat flux through the oceanic lithosphere from global heat flow. *Journal of Geophysical Research: Solid Earth*, 99(B2):3081–3095.

Stein, C. A., Stein, S., and Pelayo, A. M. (1995). *Heat Flow and Hydrothermal Circulation*, pages 425–445. American Geophysical Union (AGU).

Wallmann, K., Aloisi, G., Haeckel, M., Tishchenko, P., Pavlova, G., Greinert, J., Kutterolf, S., and Eisenhauer, A. (2008). Silicate weathering in anoxic marine sediments. *Geochimica et Cosmochimica Acta*, 72(12):2895–2918.

White, A. F. and Brantley, S. L. (2003). The effect of time on the weathering of silicate minerals: why do weathering rates differ in the laboratory and field? *Chemical Geology*, 202(3-4):479–506.

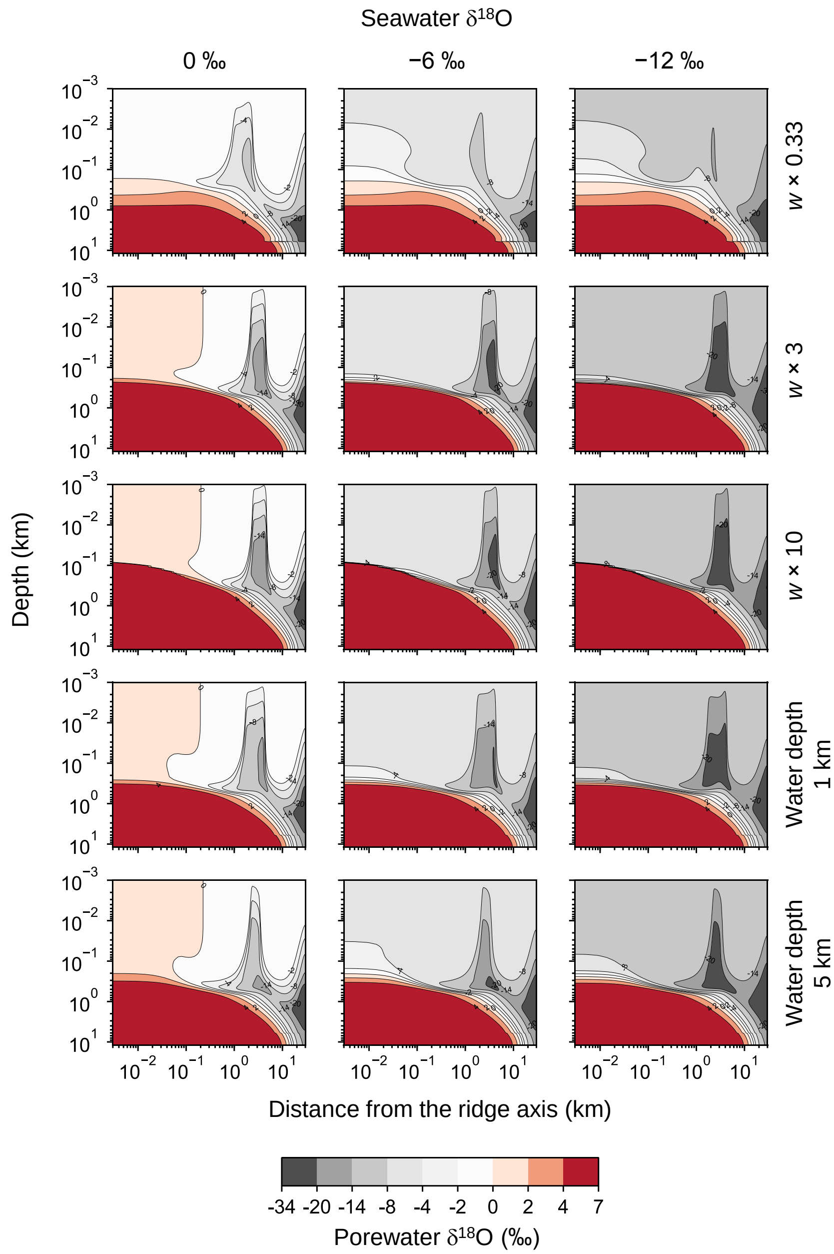

Figure S1: Two-dimensional distributions of porewater $\delta^{18}O$ at 0, −6 and −12 ‰ of seawater $\delta^{18}O$ with different spreading rates and ocean depths. The panels in the first, second and third columns assume 0, −6 and −12 ‰ of seawater $\delta^{18}O$, respectively, while those in the first, second, third, fourth and fifth rows adopt 1×10^{-2} m yr^{-1} of spreading rate, 9×10^{-2} m yr^{-1} of spreading rate, 30×10^{-2} m yr^{-1} of spreading rate, 1 km of ocean depth and 5 km of ocean depth, respectively, with other parameter values remaining the same as in the standard simulation (Sections 3.1 and 3.2).

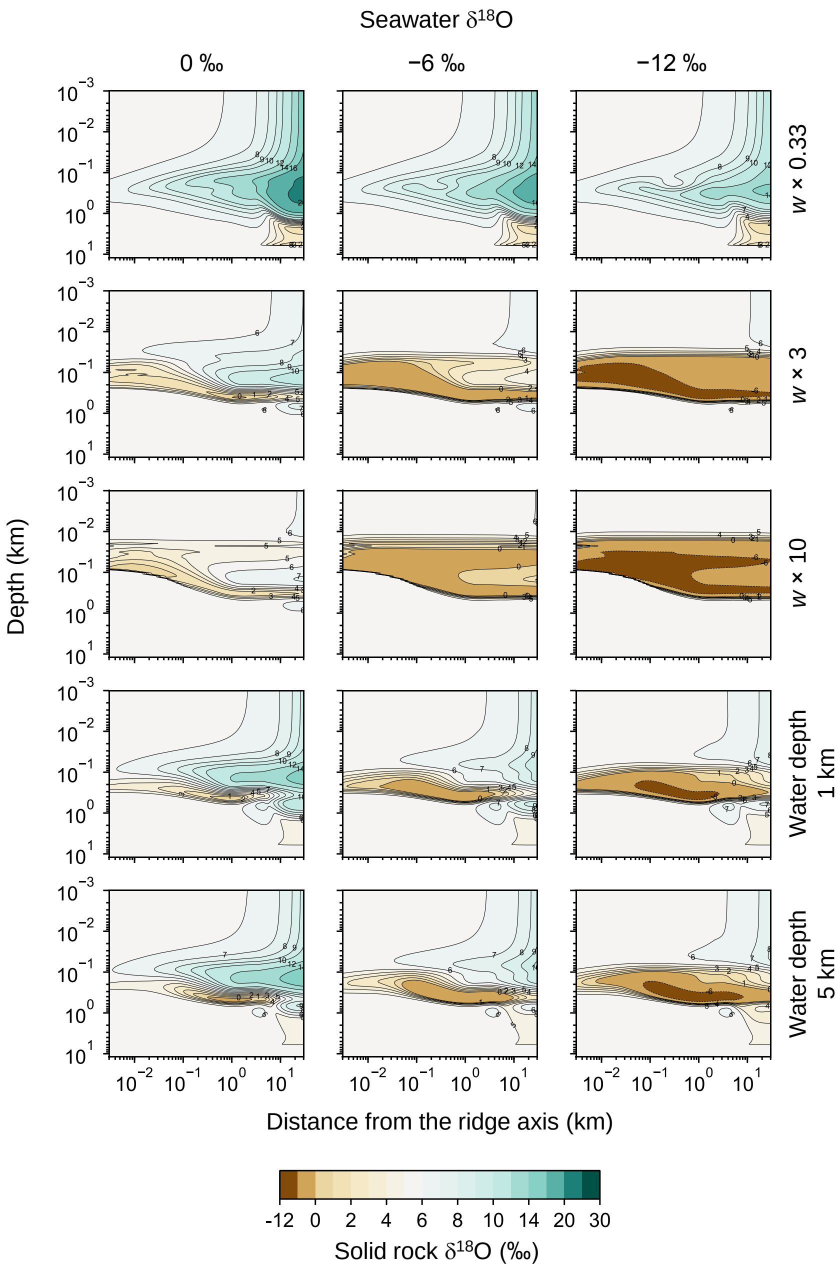

Figure S2: Two-dimensional distributions of solid rock $\delta^{18}O$ at 0, −6 and −12 ‰ of seawater $\delta^{18}O$ with different spreading rates and ocean depths. The panels in the first, second and third columns assume 0, −6 and −12 ‰ of seawater $\delta^{18}O$, respectively, while those in the first, second, third, fourth and fifth rows adopt 1×10^{-2} m yr^{-1} of spreading rate, 9×10^{-2} m yr^{-1} of spreading rate, 30×10^{-2} m yr^{-1} of spreading rate, 1 km of ocean depth and 5 km of ocean depth, respectively, with other parameter values remaining the same as in the standard simulation (Sections 3.1 and 3.2).

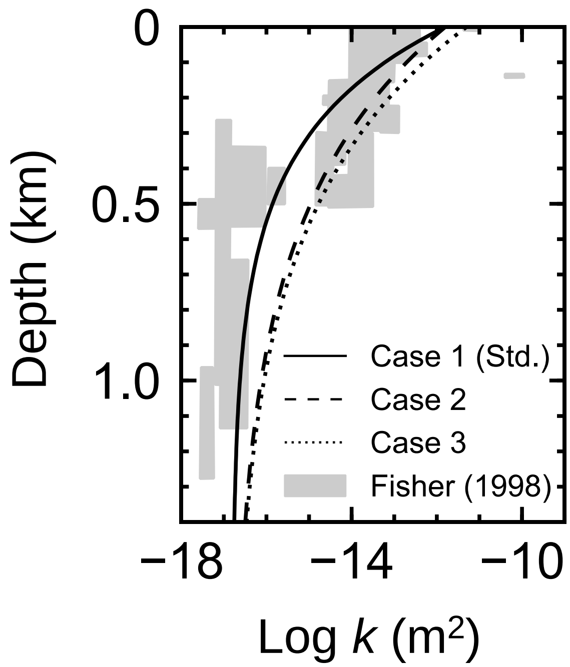

Figure S3: Permeability distributions assumed. See Section S2 for the details on cases 1–3. Gray regions show observed ranges (Fisher, 1998).

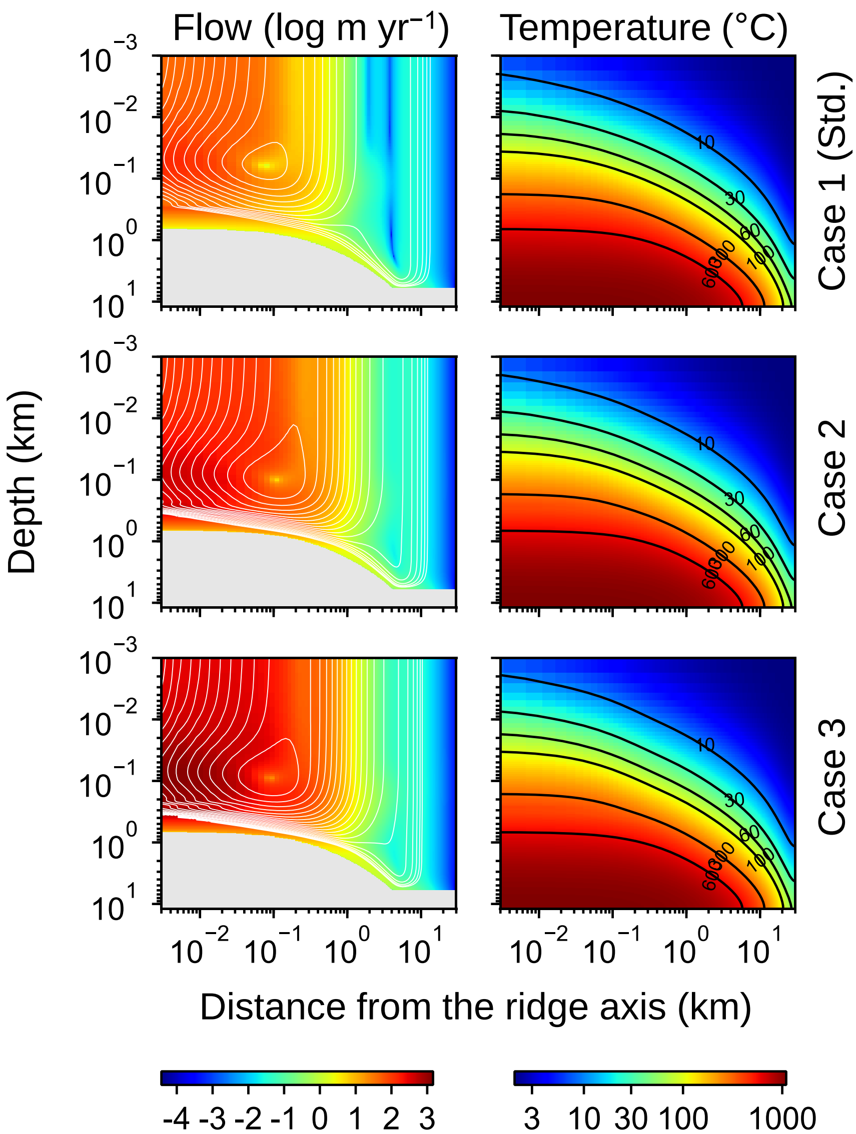

Figure S4: Two-dimensional distributions of hydrothermal fluid flow (left column) and temperature (right column) from simulations with different permeability distributions (cases 1–3 in Fig. S3; first, second and third rows, respectively). In left panels, logarithms of fluid velocity and mass-based stream lines are depicted and gray zones represent where rocks are impermeable below 6 km depth and/or with temperatures above the rock-cracking threshold (600 °C). See Section S2 for the details on cases 1–3.

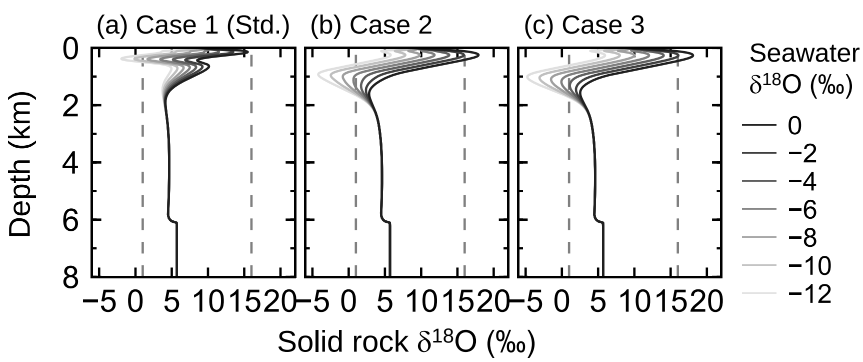

Figure S5: Solid rock $\delta^{18}O$ as function of depth at 30 km from the ridge axis with 0, −2, ..., −12 ‰ of seawater $\delta^{18}O$ from simulations with different permeability distributions (cases 1–3 in Fig. S3; a–c, respectively). Dashed lines denote 1 and 16 ‰, between which observed $\delta^{18}O$ of ophiolites and/or oceanic crust ranges. See Section S2 for the details on cases 1–3.

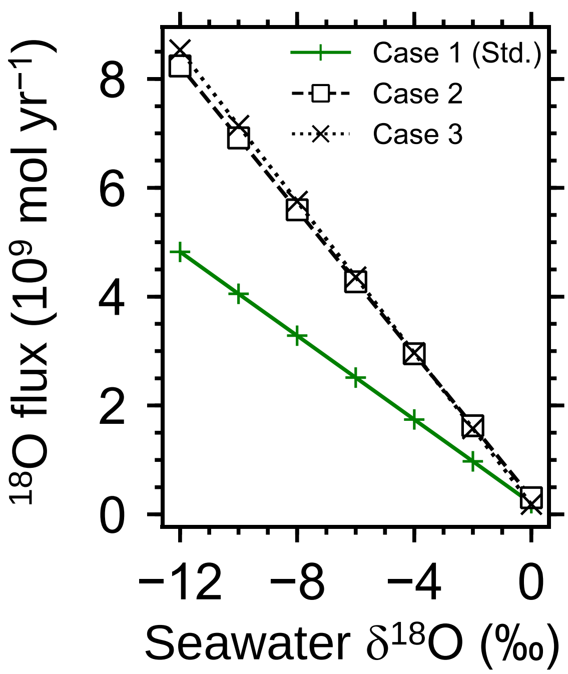

Figure S6: Net ^{18}O flux to the ocean from hydrothermal systems as function of seawater δ^{18}O from simulations with different permeability distributions (cases 1–3 in Fig. S3). See Section S2 for the details on cases 1–3.

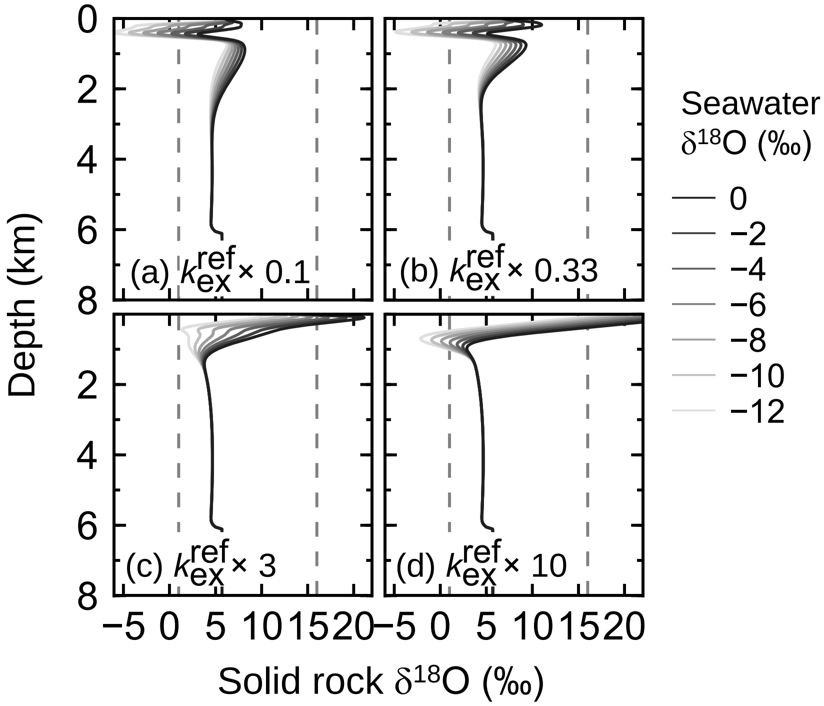

Figure S7: Solid rock δ^{18}O as function of depth at 30 km from the ridge axis with 0, −2, ..., −12 ‰ of seawater δ^{18}O from simulations with different k_{ex}^{ref} values ($\log k_{ex}^{ref} = -9.5, -9.0, -8.0$ and -7.5 mol^{-1} kg yr^{-1} in a–d, respectively). See Section S3 for more details. Dashed lines denote 1 and 16 ‰, between which observed δ^{18}O of ophiolites and/or oceanic crust ranges.

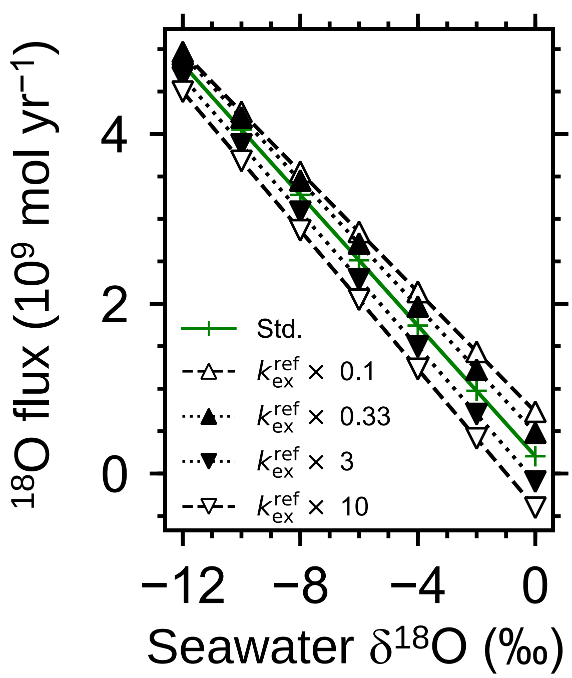

Figure S8: Net ^{18}O flux to the ocean from hydrothermal systems as function of seawater δ^{18}O from simulations with different k_{ex}^{ref} values ($\log k_{ex}^{ref} = -9.5, -9.0, -8.5, -8.0$ and -7.5 mol^{-1} kg yr^{-1}). See Section S3 for more details.

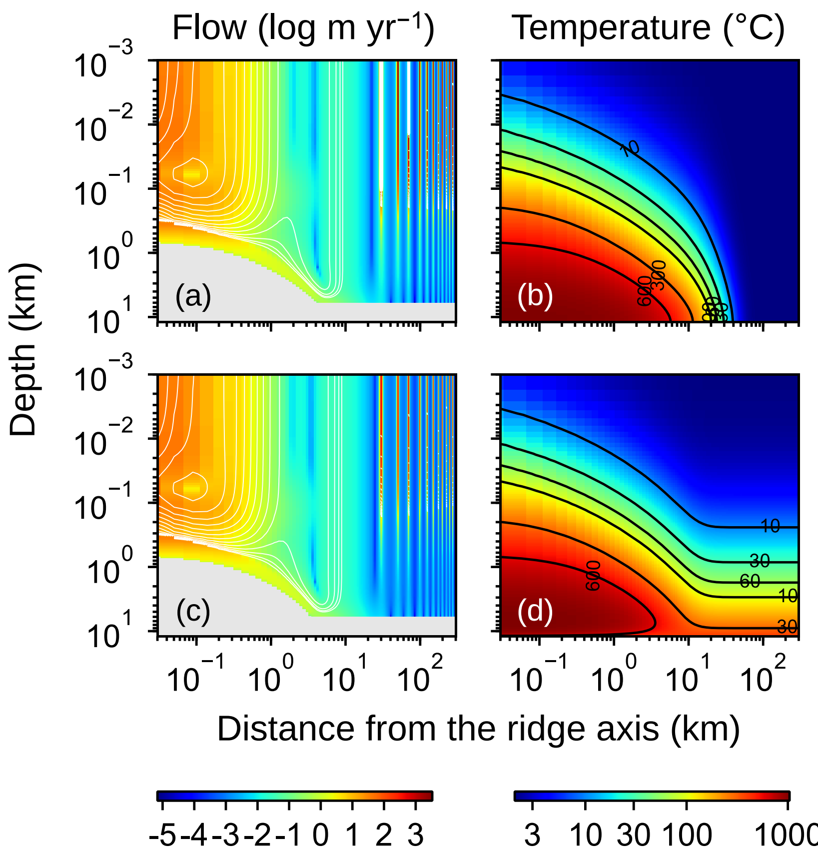

Figure S9: Two-dimensional distributions of hydrothermal fluid flow (a and c) and temperature (b and d) from off-axis experiments 1 (a and b) and 2 (c and d). In a and c, logarithms of fluid velocity and mass-based stream lines are depicted. See the caption of Fig. S4 for the explanation of gray zones in a and c. See Section S4 for the details on off-axis experiments 1 and 2.

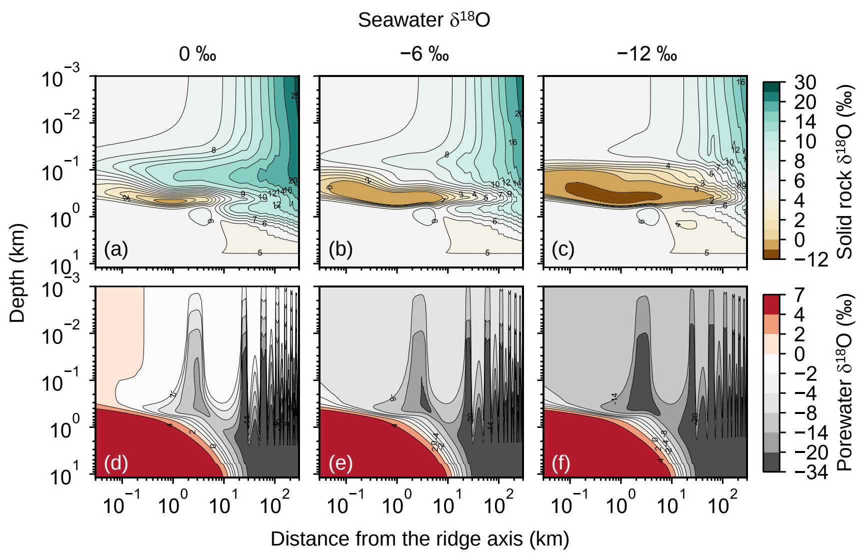

Figure S10: Two-dimensional distributions of solid-rock and porewater δ^{18}O (a–c and d–f, respectively) at 0, −6 and −12 ‰ of seawater δ^{18}O (a and d, b and e, and c and f, respectively) from off-axis experiment 1. See Section S4 for the details on off-axis experiment 1.

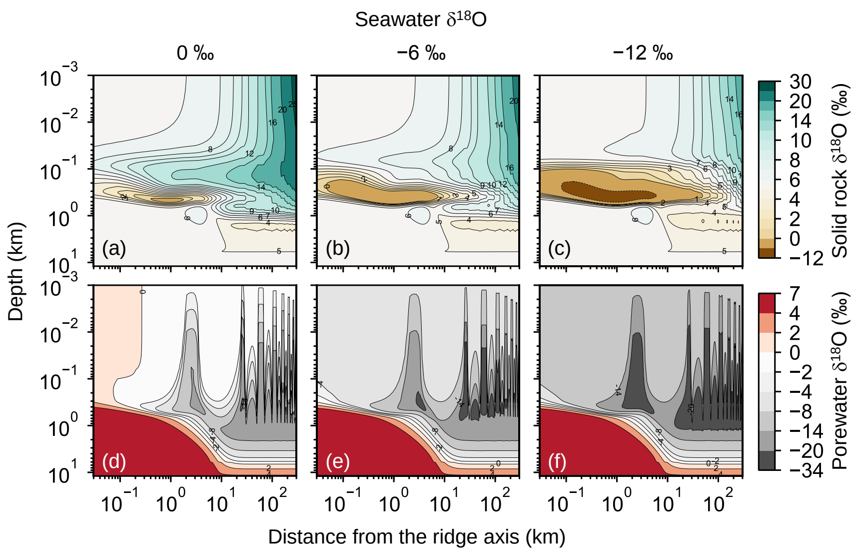

Figure S11: Two-dimensional distributions of solid-rock and porewater δ^{18}O (a–c and d–f, respectively) at 0, −6 and −12 ‰ of seawater δ^{18}O (a and d, b and e, and c and f, respectively) from off-axis experiment 2. See Section S4 for the details on off-axis experiment 2.

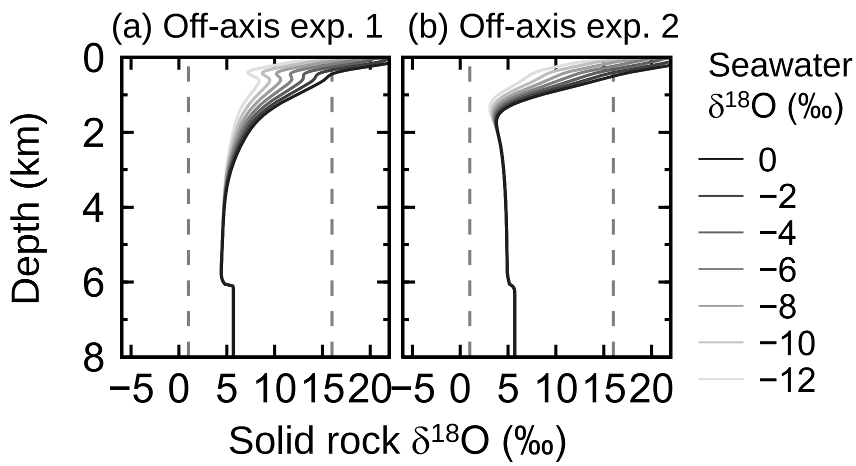

Figure S12: Solid rock δ^{18}O as function of depth at 300 km from the ridge axis with 0, −2, ..., −12 ‰ of seawater δ^{18}O in off-axis experiments 1 and 2. See Section S4 for the details on off-axis experiments 1 and 2. Dashed lines denote 1 and 16 ‰, between which observed δ^{18}O of ophiolites and/or oceanic crust ranges.

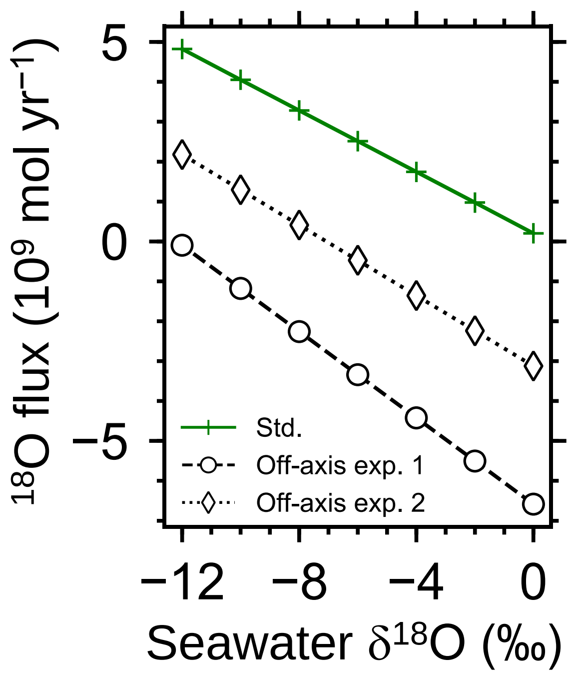

Figure S13: Net ^{18}O flux to the ocean from hydrothermal systems as function of seawater δ^{18}O from off-axis experiments 1 and 2 and the standard simulation. See Section S4 for the details on off-axis experiments 1 and 2.